Finite Element Method Simulations of the Near-Field Enhancement at the Vicinity of Fractal Rough Metallic Surfaces

Miodrag Micic,[†] Nicholas Klymyshyn, and H. Peter Lu*

Pacific Northwest National Laboratory, Fundamental Science Division, P.O. Box 999, MSIN K8-88, Richland, Washington 99352

Received: June 18, 2003

We report on (1) simulations of the influence of different surface morphologies on electromagnetic field enhancements at the rough surfaces of noble metals, and (2) the evaluations of the optimal conditions for the generation of a surface-enhanced Raman signal of absorbed species on a metallic substrate. All simulations were performed with a classical electrodynamics approach using the full set of Maxwell's equations that were solved with the three-dimensional finite element method (FEM). Two different classes of surfaces were modeled using fractals, representing dendritic and sponge-like structures. The simulations depict the high inhomogeneity of an enhanced electromagnetic field as that both a field enhancement and a field attenuation near the surface existed. While the dendritical fractals enhanced the local electromagnetic field, the sponge-like fractals significantly reduced the local electromagnetic field intensity. Moreover, the fractal orders of the fractal objects did not significantly alter the total enhancement, and the distribution of a near-field enhancement was essentially invariant to the changes in the angle of an incoming laser beam.

Introduction

The near-field optical enhancement at metal surfaces and associated phenomena, such as surface-enhanced Raman scattering (SERS),[1−12] fluorescent quenching, and enhancement,[13−17] and various near-field fluorescence-based scanning microscopies (NSOM),[12,13,18−23] all strongly depend on metallic surface properties, mainly on surface morphology and surface plasmon resonance (SPR) frequency. To achieve higher near-field enhancement of the local evanescent electromagnetic field on a metallic surface under illumination, it is favorable to have a very rough and redundant surface. High efficiency of near-field enhancement has been observed on different classes of irregular rough surfaces, such as self-affined metallic surfaces,[24] surfaces with different fractal geometries,[25] electrode surfaces,[26,27] and the surfaces of noble metal and nanoparticle clusters.[2,28−40] Due to the practical applications of electromagnetic field enhancement at rough surfaces, such as SPR and SERS spectroscopies, a plethora of experimental and theoretical works explores the origin of enhancement effects and optimized surface morphologies.[24−40]

A rough surface can be essentially described either as self-affined or self-similar. The object which is self-affined or self-similar at different dimension scales are commonly referred to as fractals.[41] Such phenomena are common in both time and space domains in various chemical systems,[42,43] such as in describing the topography and structure of different irregularly shaped interfaces of interest for catalysis.[44]

In this paper, we present our simulations of near-field electromagnetic enhancement near Au metal fractal surfaces. High near-field enhancement is a necessary ingredient for SERS and recent work in near-field SERS microscopies.[22,45−50] The most common substrates being used for such experiments are (a) rough silver or gold thin films made by vapor deposition[8] or sputter-coating, or (b) clusters of silver or gold nanoparticles[1] deposited on an inert substrate such as glass.

For modeling purposes, all surface topographies are notable for their self-similarity, i.e., their geometric behavior is best described with fractals. However, there are different kinds of fractal surfaces. For example, a metal sputter-coated substrate or a spin-coated cluster of percolated nanoparticles will result in a random, self-affined rough surface, best described as random fractals. A dendritic structure could be formed under diffusion-limited aggregations. On the other hand, a porous structure can be created as a metallic coating applied to a porous catalyst support surface. These kinds of semi-regular structures, which express similar morphological features at different scales, are examples of regular fractals. In our finite element simulation, near-field enhancement at the surface of regular fractals is generated by a coherent electromagnetic plane-wave representing the laser irradiation used in SERS experiments. The goal of the study was to provide insight into which kind of fractal surface provides the best near-field enhancement and to explore the distribution and change in near-field enhancement with various generations of the fractal iterations. All simulations were performed by classical electrodynamics approach using the full set of Maxwell's equations, solved with the three-dimensional finite element method (FEM) solver, ANSYS Multiphysics.

Models and Methods

With a gradual increase of computing power in the last three decades, there has been a significant increase in the number of finite element methods applications in microwave engineering, optics, and optical engineering,[51] and recently in nanotechnology.[50,52,53] In this work, we used FEM with a frequency domain approach and a fully enclosing three-dimensional mesh based

* Author to whom correspondence should be addressed. E-mail: Peter.Lu@pnl.gov.

[†] Current address: Veeco Instruments Inc., 112 Robin Hill Road, Santa Barbara, CA 93117.

10.1021/jp030773k CCC: $27.50
Published on Web 02/05/2004

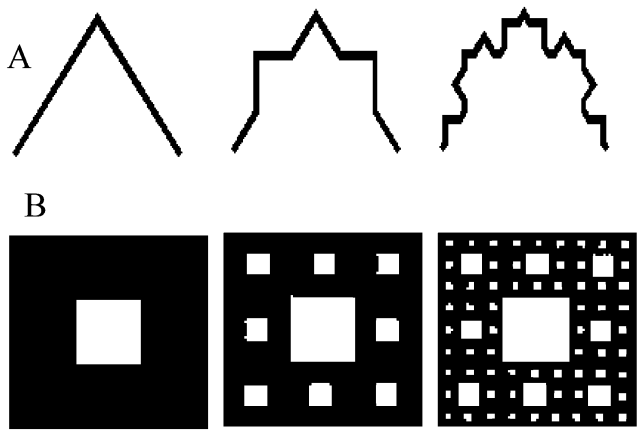

Figure 1. Schematic representation of the three-generation fractals used in our simulations: (A) Koch curve fractal is used as a basis for diffusion-limited aggregation dendritic growth surface; (B) Menger sponge fractal is used for depicting the porous surface.

on tetrahedral (first-order) elements to simulate the near-field enhancement of the fractal surfaces. Figure 1 shows the 2D representations of three-generation motifs of the regular fractal surfaces that we used to depict different repetitive rough interfaces. Figure 1A represents dendritic fractals. To model the dendritic surface, we used a three-dimensional extension of the Koch curve,[44] in which the repetitive motif is a pyramid. Figure 1B depicts volume fractals, based on the Menger sponge[44] used to describe the structure of porous surfaces. All of the regular fractal models, simulated with different generations of iteration (k) ranging from 0 to 3, have been analyzed. The field enhancement was studied in relation to the orientation of the incoming light-wave propagation vector.

The dielectric constants, which depend on the material and the excitation laser wavelength, were assumed to be uniform within the modeled surface. The mesh of the models presented here extends to 400 nm above the surface, or a half of the excitation-laser wavelength, to minimize boundary influences. The pyramidal fractal base for Koch curve-like dendritic fractals was 80 nm (height and base). The basic motif of the Manger sponge model had characteristic size of $270 \times 90 \times 30$ nm^3. Both types were matrixed in 8×8 patterns. To have reasonable accuracy in the ANSYS high-frequency electromagnetic analyses, the maximum element size anywhere in the model must be smaller than 81 nm (1/10 of the excitation wavelength at 810 nm). In the regions of interest, the smallest element size was 7 nm, and the largest elements were 40 and 80 nm in the 3D variant of Koch curve analysis and in the Menger sponge analysis, respectively. The laser beam was represented as a plane-wave for two reasons: (i) the significantly larger size of the beam in the experimental conditions ($\sim$ a few hundred nanometers) compared to the size of the fractal motifs ($\sim$80−270 nanometers); and (ii) the numerical complexities associated with modeling laser beam of a Gaussian spatial profile by FEM. The experimentally determined frequency-dependent material dielectric constants were used from an experimental measurement of noble metal thin-film optical properties.[54] The far-field radiation boundary was set up by assuming a surface impedance (Z) boundary condition of $Z = (\omega_o/\epsilon_o)^{1/2}$, wherein the ω_o is the permeability of free space, and ϵ_o is the free-space permittivity. To properly solve a high-frequency electromagnetic problem, or any electromagnetic problem in a near-field, i.e., when the size of the model is smaller than the applied electromagnetic field wavelength, a complete set of Maxwell's equations must be used. Frequency-domain FEM calculations provide the current state-of-the-art in electromagnetic FEM solvers although they require more computational power than time-domain FEM solvers need.

In our FEM simulation, a first-order tetrahedral element was used for volume discretization, which is the same as that in the previously published simulation of apertureless NSOM microscopy based on the metallic coated AFM tips.[50] Higher-order elements were tested in this situation but proved to add computation time without increasing the accuracy of the results. We used a first-order tetrahedral element in the form of a tangential vector element. Mesh generation was done directly in ANSYS Multiphysics. The highest mesh density was nearest the surfaces, and nowhere in the model did the mesh density fall below 10 elements per wavelength in any direction, as required by ANSYS for the accuracy of the numerical field solutions. In regions of high field enhancement, the mesh was progressively refined until a saturation was reached, beyond which further mesh refinement did not affect the results. All material constants depicting the Au ($\epsilon = -24.9 + 1.57i$) and the 810-nm laser excitation at surface-plasmon resonance frequency were used in the simulations.

Results and Discussion

The surface roughness can be modeled as three-dimensional patterns. Fractal theory has revealed that many patterns possess scaling symmetry, i.e., self-similarity at different scales. Scalability can be geometrical, as in regular fractals, or statistical, as when the statistical distribution has the same properties over different scales. The "yardstick" for measuring the scalability could be line, surface, mass, or time. To simulate enhancement of the local electromagnetic field in the vicinity of rough surfaces, we have used Menger sponge fractal as a model of porous surface, and a 3D extension of the Koch curve fractal as an approximation for surface with dendritic growth. The Koch curve recursive algorithm has been applied on square-based pyramids, wherein the recursion occurs with growing of the smaller, 1/4 of original size, pyramid at the 1/3 of the heights of the vertex surface. Such a model can accurately depict the semi-regular masses of dendritic growth on noble metal surfaces, which are most commonly used in the SERS active substrate.

I. The Near-Field Enhancement of the Au Dendritic Fractal Surface. With its unique capability of identifying molecules, Raman spectroscopy is one of the most promising microscopic analytical techniques. Furthermore, its practical application is often associated with SERS. The strong surface enhancement of the Raman active substrates acts as leverage for Raman signals, increasing the signal intensity and the chemical detection sensitivity. Most SERS-active substrates are rough metallic surfaces, especially Ag and Au. Electrodeposition at a surface occurs when the diffusion-limited aggregation forms structures resembling dendritic fractal growth, which are responsible for the surface roughness. However, such structures cannot be defined as true regular fractals because redundant self-similarity is not necessarily established across scales and is limited by the mechanical stability of the grown dendrites. Such structures are defined as pseudo- or pre-fractals.[55] There are extreme cases of self-similarity of electrochemical dendritic structures in size ranges from centimeters to nanometers,[56] but such structures are extremely fragile and unsuitable for most of the SERS experiments or as field-enhancement fractal antennas. The surface roughness of the typical regular-fractal surfaces is usually in the range of tens of nanometers to the tens of micrometers.

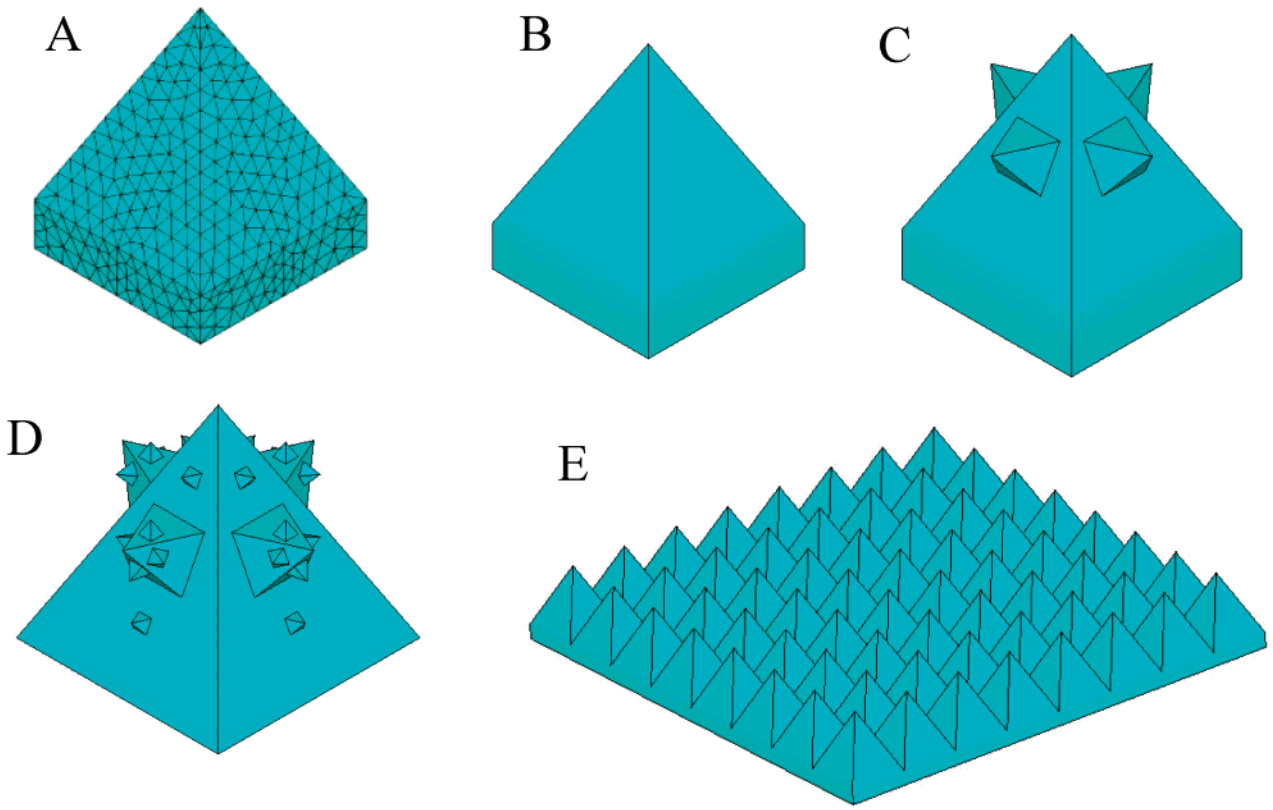

Figure 2. Solid models used to generate finite element mesh of the simulated diffusion-limited aggregation-grown dendrites at different generations: (A) and (B) first order, (C) second order, and (D) third order generation of fractals based on three-dimensional representation of the Koch curve. (E) Full-scale surface model of first order fractal.

To simulate the effects of surface roughness on near-field enhancement, a three-dimensional representation of the Koch curve was generated for dendrites of different orders. The Koch curve model comprised a square-based pyramid, grown interactively by scaling its dimension to 1/4 of the initial size and positioning the base center at the centroid of the sides (Figure 1A). Fractals of first, second, and third orders have been simulated. Higher-order fractals were not considered due to the increasing complexity and computational cost. The simulated surface consists of matrix of 8×8 closely packed Au-based fractal structures of first, second, and third orders. The side of the base of the foundation fractal class pyramid is 80 nm. Figure 2 presents three-dimensional finite element meshes of the generated fractal geometries. The laser excitation at 810 nm has been applied as a plane-wave electromagnetic wave propagating under 0, 45, and 90 degrees relative to the horizontal substrate surface.

Figure 3A,B represents simulation results of the first-order fractal under 45 degrees of incoming laser beam illumination. The first-order fractal model consisted of the topographic grid of the regular square-based pyramid. The lightning-rod effect is clearly observable, with the ~3-fold enhancement concentrated at the tips of the pyramids. The distribution volume of the local field enhancement is constrained within about 10 nm from the surface around the tips of the pyramids. In contrast, the electromagnetic field is significantly depleted at the bottom of the pyramids, as well as in the interstitial spaces. The field depletion in the interstitial space is an interesting observation, which suggests that in the regular topographic grid-like structure, the Raman signal will be predominately produced from the molecules located only within the volume of the hot spots at the apexes of the dendrites. Such inhomogeneous field enhancement results in just part of the adsorbed molecules being optically active, which explains the large fluctuation of SERS spectra at a hot spot on the substrates covered with ultra-diluted optically active molecules, for example, the "single-molecule" SERS.[10,33−40] By varying the incoming laser beam incident angle from 0° to 90°, we observed no significant change in the absolute intensity and distribution shape of the near-field enhancement in the surface vicinity. Thus, on the densely populated surface with dendrites of fractal geometry, the near-field enhancement is insensitive to the direction of incoming laser beam propagation vectors.

The next level of iteration, the fractal of second order results, is depicted in Figure 4. Figure 4A is a cross-section through the model, while Figures 4B and 4C represent top-view cross-sections, at the level of the top apex of the main dendrite pyramid (Figure 4B) and at the level of the top apex of the side-grown pyramids (Figure 4C). Results in this fractal are similar to those of the regular topographic matrix. It was logical to expect that the side-grown dendritic structure would also act as a field enhancer. However, the simulation shows that the enhancement is concentrated in a small volume around the highest apex of the dendritic structure, in a winner-take-all, lightning rod manner, with a 3-fold enhancement. Similar to the previous case, the enhancement volume and intensity are essentially invariant given the direction of the laser beam polarization vector, and the large field depletion is observed in the interstitial space, below the top apex of the pyramid, all the way to the bottom. Figure 4B shows that there is negligible effect of the smaller dendritic side-growth, which has no influence on the total field enhancement.

Figures 5A and 5B represent fractals of the third order of iterations. The same effects are observed as that in the second order fractal, with the winner-take-all, lightning rod effect dominating the near-field enhancement at the highest apex of

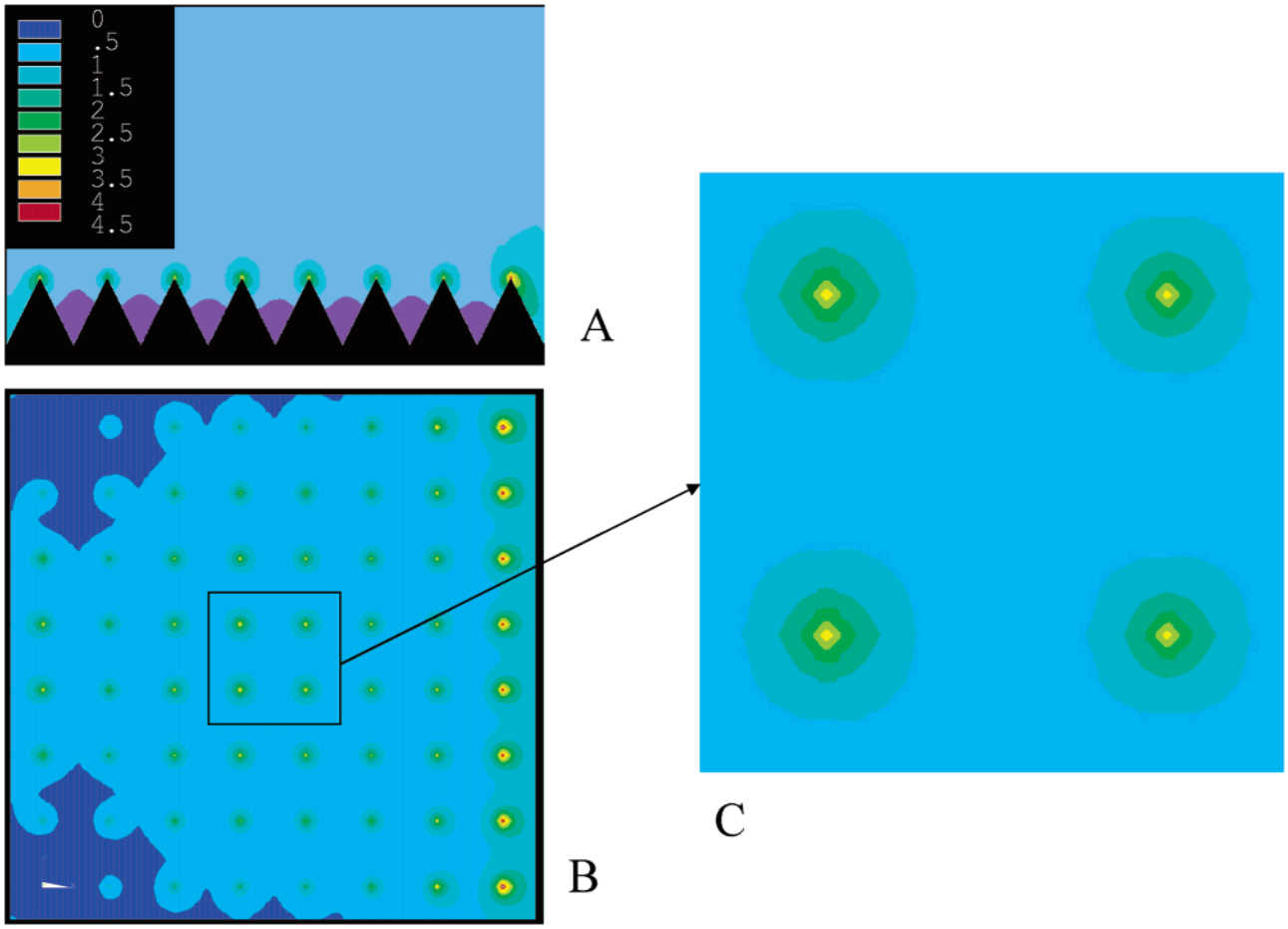

Figure 3. Near-field enhancement distributions of the first-order generation simulations of a dendritic surface, Au in a vacuum, irradiated with 810-nm plane-wave at 45° propagation: (A) side-view cross-section of the three-dimensional model; (B) top-view cross-section of the three-dimensional model, at the level of top apex; (C) top-view zoom in of the model central area without boundary condition influence.

the dendrite and with strong field attenuation elsewhere. The same invariance to the propagation of the incoming light is observed as in the previous cases, with a similar total intensity of a 3-fold enhancement.

From a previous simulation of single metallic tips, it was known that near-field enhancement is strongly dependent on the incoming field propagation and polarization vectors.[50,53,57−61] To investigate if the observed invariant behavior of the fractal surface originated from the packing, we simulated single isolated third-order dendrites under 45° laser beam illumination (Figure 6). The single dendrite structure has lower overall near-field enhancement (about 2.6 times) and a larger volume of the field enhancement. The observed volume is uniformly overcasting the highest dendritic vertices. This simulation confirms our hypothesis that the packing is the ultimate source of the winner-take-all effect and leads to the slight increase in the total enhancement. The increase in total enhancement in packed dendrites, as opposed to single dendrites, could be explained by the field concentration in the smaller volume, leading ultimately to the higher enhancement. This implies that the strong Raman line enhancements originate from the constrained volumes. Due to the spatial inhomogeneity of the generated near-field, which is mainly concentrated at the top of the dendrites, most of the Raman signals of the molecules absorbed on the surface will not be enhanced by the surface. Furthermore, in a case of surface sparsely populated with absorbed species, the molecules are capable of moving on the surface by different diffusion mechanisms. Therefore, molecules can diffuse in and out of the regions of high enhancement, an effect that will produce large Raman spectra fluctuations, as reported previously by our experimental research[62] and other groups.[31−40] The magnitude of fluctuations can be significant, especially due to the well-accepted simple presumption that the SERS signal is proportional to the fourth power of the electric field strength[1,31−40,62]

II. The Near-Field Attenuation of Porous Surfaces. The interesting property of volume fractals is that the volume of their features will asymptotically approach zero as the generation of iteration approaches infinity. Examples of such a model are ceramic catalytic supports, various aero gels, and porous silica. These highly porous materials could be coated with metals. Our simulation is to explore the possibility of forming a strongly SERS-active substrate by coating such materials with noble metals, particularly with Ag and Au. In this study, we used one side of the Menger sponge to represent the porous surfaces, as it is a common model for the catalyst supports.[44] The fractal used in our simulation is the third generation of iteration. The mesh was generated by iterative subtraction of boxes, with size ratios of 1/3 from the solid metallic surface. The Menger sponge was generated just on one side of the surface, and the motif fractal of the third generation fractal was multiplied in an 8 × 8 pattern. The detail of the finite element mesh of this particular model is shown in Figure 7A. We modeled for excitations at vertical, 45°, and horizontal laser beam propagation.

Results of simulation for the 45° laser beam propagation are presented by showing the cross-section through the model close

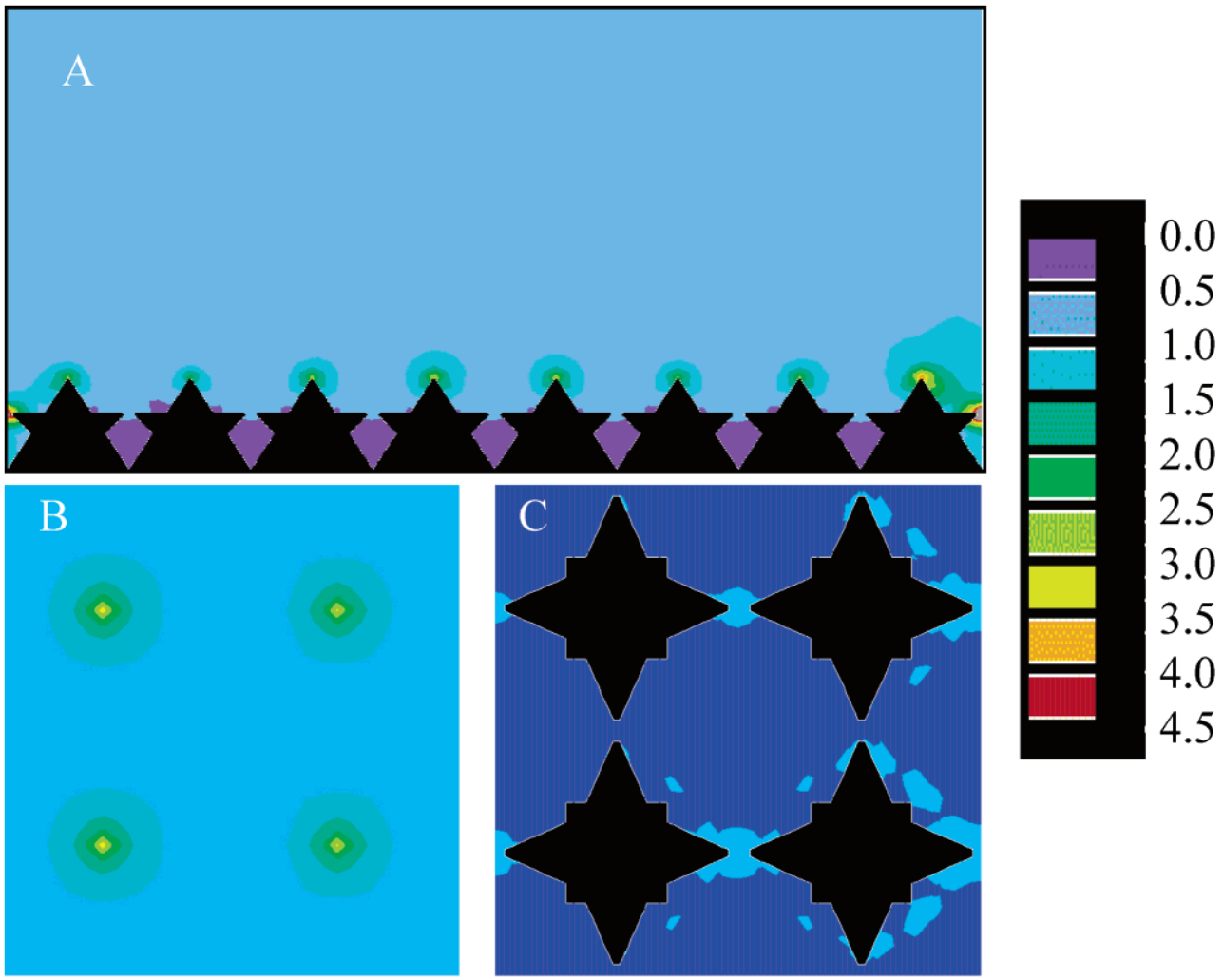

Figure 4. Near-field enhancement distributions of the second-order generation simulations of dendritic surface, Au in a vacuum, irradiated with 810-nm plane-wave at 45° propagation: (A) side-view cross-section of the three-dimensional model; (B) top-view cross-section of the three-dimensional model, at the level of top apex; (C) top-view cross-section at the level of smaller dendritic apexes.

to the Au surface (Figure 7B). As with previous dendritic fractals, the local electric field seems to be essentially insensitive to the direction of the incoming laser beam propagation, which is the unique property of fractals. The enhancement factor variation in all three simulations was within the range of the numerical error of the FEM solver. In the Menger sponge fractal, instead of the electric near-field enhancement, we observed strong near-field depletion, in the range of an order of magnitude in a close proximity to the metal surface. The electric field attenuation is strongest within the pore, which could be explained partially in terms of the "Faraday cage" effect. The Menger sponge acts as a very broadband attenuator, i.e., the same behavior is observed over the range of wavelengths. The observed behavior is consistent with experimental investigations of the return loss of volume antennas[63] where the large return loss in the range of the −20 to −40 dB has been measured in the microwave frequency range (1−20 GHz) from the printed fractal volume micro-strip antenna. The experimentally observed effect of the polarization perturbation, typical for the fractal antenna, can be used to explain the results in the simulation of the irrelevance of incoming laser beam polarization vector directions. The simulations explain why highly porous materials, such as catalyst support, will not act as effective SERS substrates. The near field on the surface of such material will be significantly attenuated so that the generated SERS signal will be insignificant.

III. Limitations of the FEM Simulations and Some Possible Improvements. The large-scale simulations in this study were at the border of our computational limitation. When solving a potential problem utilizing a finite-size numerical model, the accuracy of the model will be significantly influenced by the appropriate selection of the physical size, volume discretization, boundary conditions, and mesh density. Practically, with an increase of model size and mesh density, there is a dramatic increase in demands for computational resources. Therefore, it is especially important for such large models, such as our models of fractal surfaces, to have an optimal mesh density and optimal size of the integration volume. The most significant advantage of the finite element method over the finite difference methods and other numerical procedures is in the nonuniformity of the element sizes and locally enhanced mesh densities at the point of interests. In the case of the fractals in this work, a computationally viable model was achieved with a carefully optimized mesh, allowing an increase in mesh density only in an area of interest, such as the vicinity of dendrites, and applying a simultaneous decrease of mesh density near boundaries. Even with such large model sizes, the models still suffer from the influence of boundary conditions, and a further expansion of the model was practically not accessible within our current computational constraints.

We estimated the numerical error and the magnitude of the distortion influence of boundary conditions on the calculated

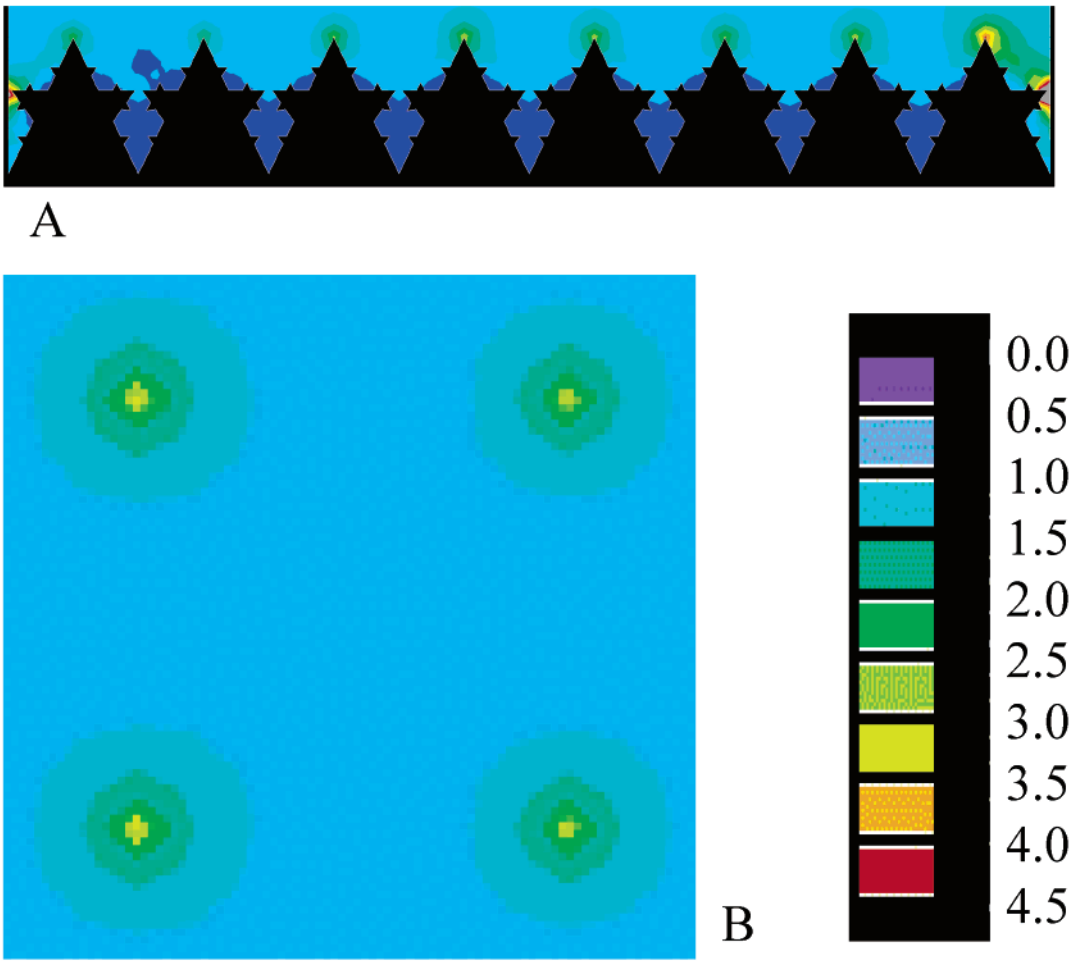

Figure 5. Near-field enhancement distributions of the third-order generation simulations of dendritic surface, Au in a vacuum, irradiated with 810-nm plane-wave, at 45° propagation: (A) side-view cross-section of the three-dimensional model; (B) top-view cross-section of the three-dimensional model, at the level of top apex; (C) top-view cross-section at the level of smaller dendritic apexes.

electromagnetic field distribution. A flat Au surface, of the same size and mesh density as the fractal models, was simulated under plane-wave irradiation at a 45° incident angle. Figure 8 depicts the boundary effect on the simulated near-field enhancement distribution, for which the electric field was expected to be of unit intensity. The electric field distortion is evident in the corners and in boundary areas up to about 1/4 of the length of the model side (Figure 8).

Although the FEM simulation is more versatile than other computational methods for solving the electric field distribution, such as MMP,[58] DDA,[60] finite differences,[57,59,61] finite elements time domain,[53] and finite element frequency domain[50] simulations, a careful consideration of its limitations must be applied before drawing definite conclusions. The main drawback of any Maxwell-equation-based methodology in nanotechnology is its assumption of a continuum "ether" space, i.e., its classical theoretical electrodynamics approach. While classical electrodynamics works well for the "big objects" such as antennas, lightning rods, microwave waveguides, and similar systems, its applicability at the small scale, those approaching molecular scales, must be carefully evaluated. In this case, the FEM simulation was employed at the scale of several tens of nanometers in order to obtain the three-dimensional intensity distribution of an evanescent electric field. In the presented simulations, it was assumed that the SERS signal is proportional to the fourth power of the excitation electric field strength. Thus, in the FEM simulations there was no estimation of the contribution of quantum mechanical effects, such as the chemical enhancement of a Raman signal, and no explicit treatment of the surface plasmon (except for the complex material constant) or other surface phenomena.[31−40,64] The macroscopic electrodynamic limitations of FEM simulation make it difficult to solve field-scattering problems from a single molecule. Although we can assume that an element much smaller than 1 nm can have a different set of dielectric constants, the results obtained will not be representative. This is because the other effects at that spatial scale, e.g., the electronic interaction of the field with the molecular orbitals, are much more highlighted, which is typically not the case with fields several tens or hundreds of nanometers larger. At a molecular and smaller scale, the use of finite elements and other classical electrodynamics methods of solving potential field problems are useful only up to the dimension-limit of the quantum scale effects, i.e., when the encompassing volume is much higher than the volume of the single molecule of interest. It is possible to couple Maxwell's macroscopic electrodynamics models and Schroedinger equations for the purpose of simultaneous solution,[65,66] thus coupling classical and quantum models. Such sophisticated model has been recently applied, in simplified analytical form, for the modeling of the effect involved in the scanning near-field exciton microscopy.[67] The electromagnetic field, as a driving force, is responsible for many effects at the molecular and atomic scale, which can be described only at the quantum level of theory. An effective way of studying surface enhancement and plasmonics effects is to use macroscopic FEM to calculate electromagnetic fields at a larger scale, e.g., several tens of

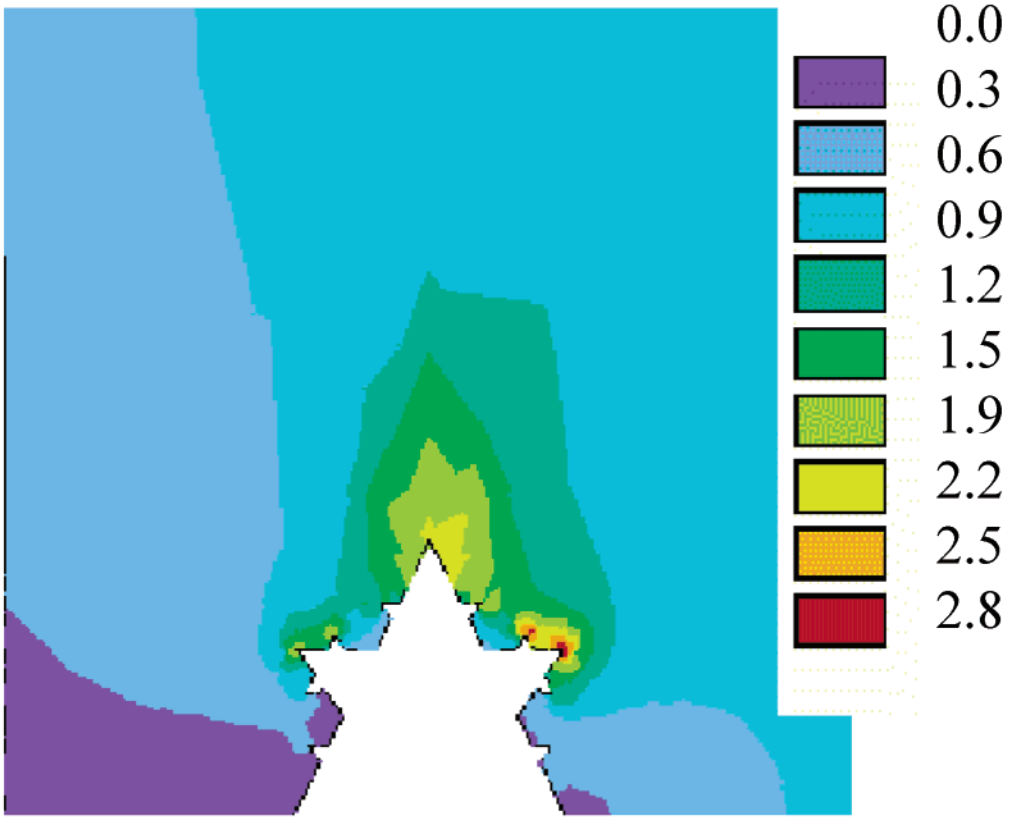

Figure 6. Near-field enhancement distributions of the third-order generation simulations of the single dendritic surface. Results represents side-view cross-section of the three-dimensional model.

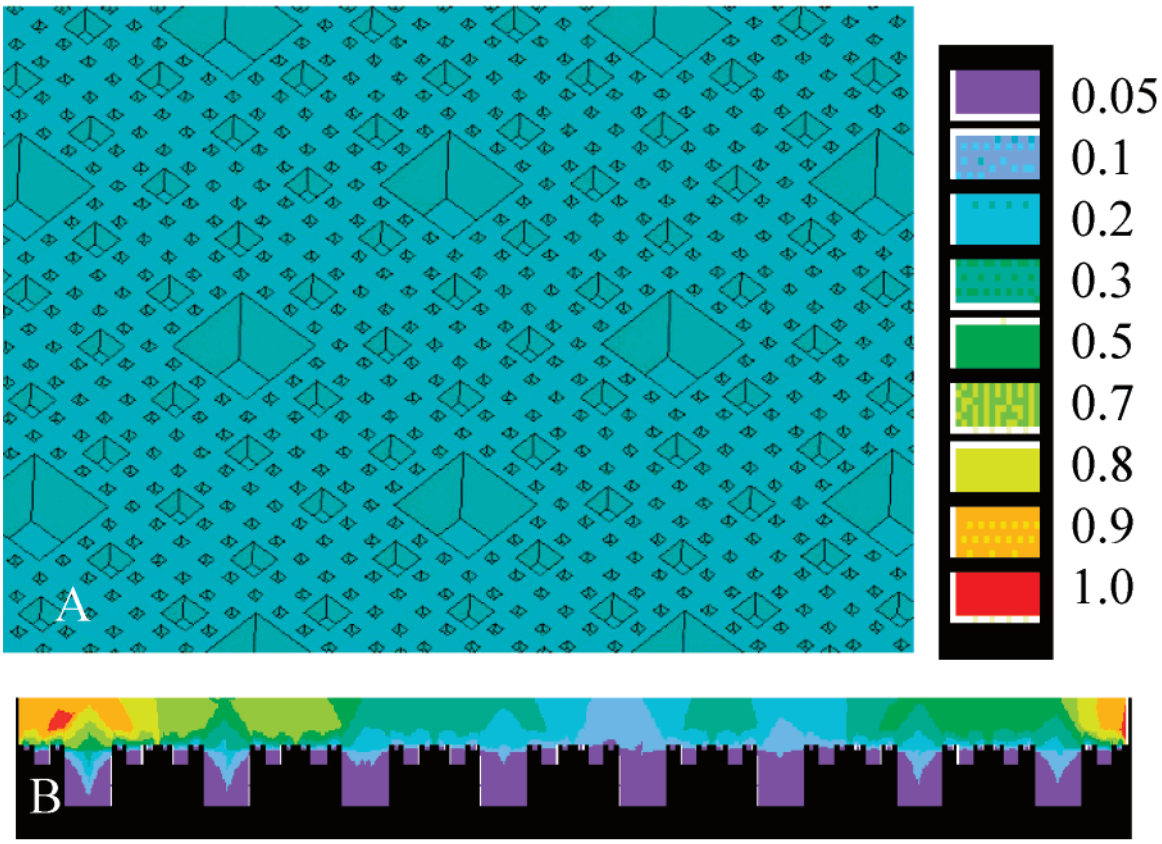

Figure 7. Near-field enhancement distributions of the third-order generation simulations of adsorber surface: (A) finite-element mesh model, (B) cross-section through the center of the model.

nanometers, and then to export results to molecular modeling that can take into account quantum-level properties and behaviors of observed molecules, such as the electronic orbital−electric field interactions.

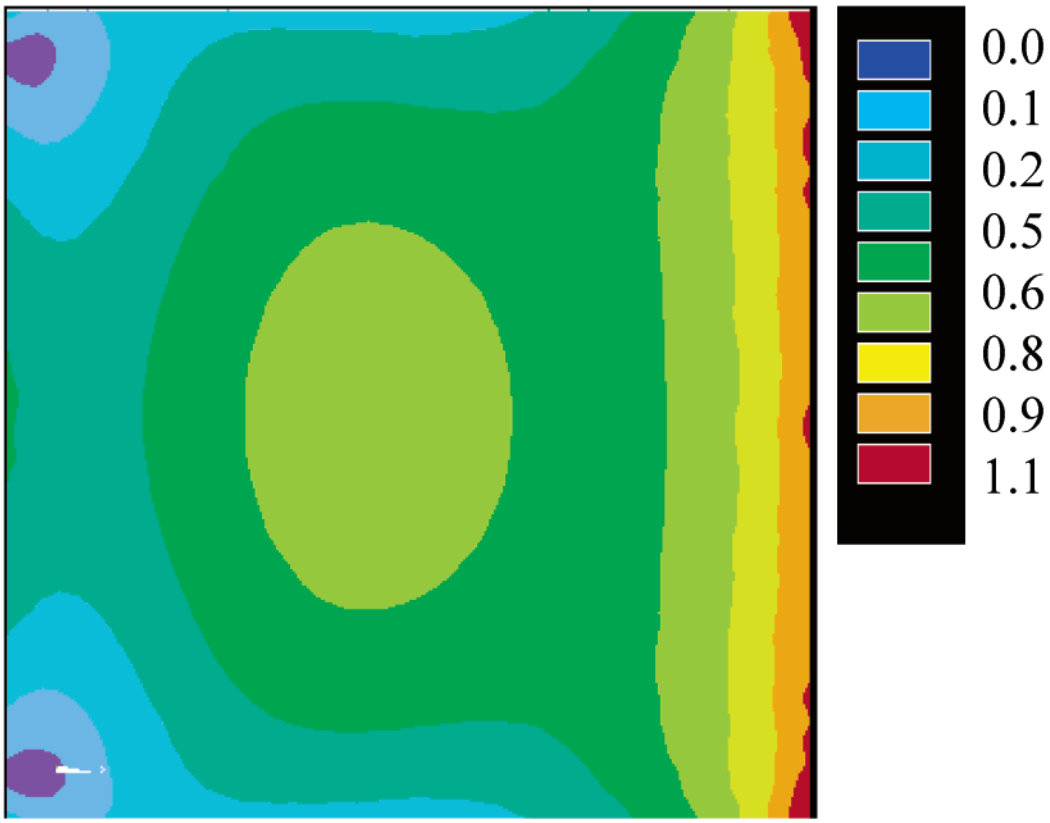

Figure 8. Near-field enhancement distribution of a perfectly flat metallic surface. Boundary artifacts are shown explicitly.

Conclusions

The FEM simulations presented here clearly demonstrate the origin of the different behaviors of evanescent near-field generation in the two main classes of the fractal-model described rough metallic surfaces: dendritic and porous surfaces. To generate field enhancement, a point-attractor is necessary. Therefore, the dendritic aggregates provide the near-field enhancement, whereas the pure absorber, i.e., a porous surface with only "cavities" in it, provides strong field attenuation. The same effect has been observed previously in simulation of random self-affined fractals.[68] On the other hand, in the porous surface, it is reasonable to explain field attenuation by the concept that the absorber cavities act like Faraday's cage so that the near-field in the volume of the cavity is depleted. In the case of closely packed dendritic aggregates, the volume of the near-field enhancement is concentrated around the highest apexes of the fractal aggregates, as the field distribution occurs in a kind of a winner-take-all or lightning rod effect. The near-field enhancement on the fractal surface has been shown to be essentially independent from the direction of electromagnetic plane wave incident angles based on the results of the enhancement simulations with varying laser incident angles in the range of 0° to 90°. Furthermore, the higher generation of the dendrite fractals does not give significantly higher near-field enhancement compared to that from first-order dendritic fractal surfaces.

There is nevertheless a large inhomogeneity in the near-field distribution in the vicinity of the rough metallic surfaces. This is especially important in considering the results of the SERS experiments of highly diluted samples as well as of single molecules. Most of the area at the bottom of surfaces is actually field-depleted where the molecules will not only have no surface enhancement but also have depleted excitation. It is most likely that the SERS signal detected from the far field is dominated by the molecules located on the tops of the dendritic apexes on the surface, with little or no contribution from the molecules in the grooves or cavities of the rough surface. Only the molecules that are absorbed close to the high apexes of dendritic aggregates will be exposed to an electric field of sufficient strength to make them SERS-active. As the molecules are capable of diffusing on the metallic surface, molecules will be constantly going in and out of the volume of the high electric near-field enhancement. This may be the significant contributor to the experimentally observed Raman fluctuations.[31−40,62,64] This conclusion is not only pertinent to single-molecule SERS but also to natural molecule thermal motion and the nonuniform evanescent field distributions in nanoscale topographic inhomogeneities in general. The results of our simulations have implications for the future apertureless near-field probe and other optically active scanning probe tips. From the simulations of the single dendrites of different generations, it could be concluded that the complex geometries of the surface skin of the scanning probe tip will not significantly improve or alter the near-field distribution intensity or pattern.

Acknowledgment. We thank Steven Barlow and Steven Colson for helpful discussions. This work was supported by the Chemical Sciences Division of the Office of Basic Energy Sciences within the Office of Energy Research of the U.S. Department of Energy (DOE).

References and Notes

(1) Moskovits, M.; Tay, L. L.; Yang, J.; Haslett, T. *Top. Appl. Phys.* **2002**, *82*, 215.
(2) Kneipp, K.; Kneipp, H.; Itzkan, I.; Dasari, R. R.; Feld, M. S. *Chem. Rev.* **1999**, *99*, 2957.
(3) Campion, A.; Kambhampati, P. *Chem. Soc. Rev.* **1998**, *27*, 241.
(4) Michaels, A. M.; Jiang, J.; Brus, L. *J. Phys. Chem. B* **2000**, *104*, 11965.
(5) Muniz-Miranda, M. *J. Raman Spectrosc.* **2002**, *33*, 295.
(6) Otto, A. *J. Raman Spectrosc.* **2002**, *33*, 593.

(7) Pettinger, B.; Picardi, G.; Schuster, R.; Ertl, G. *Single Molecules* **2002**, *3*, 285.
(8) Saito, Y.; Wang, J. J.; Smith, D. A.; Batchelder, D. N. *Langmuir* **2002**, *18*, 2959.
(9) Shibamoto, K.; Katayama, K.; Fujinami, M.; Sawada, T. *Rev. Sci. Instrum.* **2003**, *74*, 910.
(10) Xu, H. X.; Aizpurua, J.; Kall, M.; Apell, P. *Phys. Rev. E* **2000**, *62*, 4318.
(11) Zeiri, L.; Bronk, B. V.; Shabtai, Y.; Czege, J.; Efrima, S. *Colloids Surf., A—Physicochem. Eng. Aspects* **2002**, *208*, 357.
(12) Osawa, M. *Top. Appl. Phys.* **2001**, *81*, 163.
(13) Bian, R. X.; Dunn, R. C.; Xie, X. S.; Leung, P. T. *Phys. Rev. Lett.* **1995**, *75*.
(14) Ditlbacher, H.; Krenn, J. R.; Felidj, N.; Lamprecht, B.; Schider, G.; Salerno, M.; Leitner, A.; Aussenegg, F. R. *Appl. Phys. Lett.* **2002**, *80*, 404.
(15) Andrew, P.; Barnes, W. L. *Phys. Rev. B* **2001**, *6412*.
(16) Geddes, C. D.; Lakowicz, J. R. *J. Fluoresc.* **2002**, *12*, 121.
(17) Levi, S. A.; Mourran, A.; Spatz, J. P.; van Veggel, F. C. J. M.; Reinhoudt, D. N.; Moller, M. *Chemistry—A European Journal* **2002**, *8*, 3808.
(18) Trabesinger, W.; Kramer, A.; Kreiter, M.; Hecht, B.; Wild, U. P. *Appl. Phys. Lett.* **2002**, *81*, 2118.
(19) Hu, D.; Micic, M.; Klymyshyn, N.; Suh, Y. D.; Lu, H. P. *Rev. Sci. Instrum.* **2003**, *74*, 3347.
(20) Courjon, D. *Near Field Microscopy and Near Field Optics*, 1st ed.; Imperial College Press: London, 2003.
(21) Ohtsu, M. *Near-Field Nano/Atom Optics and Technology*, 1st ed.; Springer-Verlag: New York, 1998.
(22) Hayazawa, N.; Inouye, Y.; Sekkat, Z.; Kawata, S. *J. Chem. Phys.* **2002**, *117*, 1296.
(23) Kwak, E. S.; Kang, T. J.; Bout, D. A. V. *Anal. Chem.* **2001**, *73*, 3257.
(24) Douketis, C.; Haslett, T. L.; Wang, Z.; Moskovits, M.; Iannotta, S. *J. Chem. Phys.* **2000**, *113*, 11315.
(25) Bozhevolnyi, S. I.; Vohnsen, B.; Zayats, A. V.; Smolyaninov, I. I. *Surf. Sci.* **1996**, *356*, 268.
(26) Yamaguchi, Y.; Weldon, M. K.; Morris, M. D. *Appl. Spectrosc.* **1999**, *53*, 127.
(27) Rinne, C. L.; Hren, J. J.; Fedkiw, P. S. *J. Electrochem. Soc.* **2002**, *149*, C150.
(28) Brouers, F.; Rauw, D.; Clerc, J. P.; Giraud, G. *Phys. Rev. B* **1994**, *49*, 14582.
(29) Matsushita, M.; Hayakawa, Y.; Sawada, Y. *Phys. Rev. A* **1985**, *32*, 3814.
(30) Shubin, V. A.; Kim, W.; Safonov, V. P.; Sarychev, A. K.; Armstrong, R. L.; Shalaev, V. M. *J. Lightwave Technol.* **1999**, *17*, 2183.
(31) Bjerneld, E. J.; Foldes-Papp, Z.; Kall, M.; Rigler, R. *J. Phys. Chem. B* **2002**, *106*, 1213.
(32) Eggeling, C.; Schaffer, J.; Seidel, C. A. M.; Korte, J.; Brehm, G.; Schneider, S.; Schrof, W. *J. Phys. Chem. B* **2001**, *105*, 3674.
(33) Kneipp, K.; Wang, Y.; Kneipp, H.; Itzkan, I.; Dasari, R. R.; Feld, M. S. *Phys. Rev. Lett.* **1996**, *76*, 2444.
(34) Kneipp, K.; Wang, Y.; Kneipp, H.; Perelman, L. T.; Itzkan, I.; Dasari, R. R.; Feld, M. S. *Phys. Rev. Lett.* **1997**, *78*, 1667.
(35) Michaels, A. M.; Nirmal, M.; Brus, L. E. *J. Am. Chem. Soc.* **1999**, *121*, 9932.
(36) Michaels, A. M.; Jiang, J.; Brus, L. E. *J. Phys. Chem. B* **2000**, *104*, 11965.
(37) Moyer, P. J.; Schmidt, J.; Eng, L. M.; Mexiner, A. J. *J. Am. Chem. Soc.* **2000**, *122*, 5409.
(38) Nie, S.; Emory, S. R. *Science* **1997**, *275*, 1102.
(39) Xu, H.; Bjerneld, E. J.; Kall, M.; Borjesson, L. *Phys. Rev. Lett.* **1999**, *83*, 4357.
(40) Xu, H.; Azipurua, J.; Kall, M.; Appel, P. *Phys. Rev. E* **2000**, *62*, 4318.
(41) Mandelbrot, B. B. *Science* **1998**, *279*, 783.
(42) Rothschild, W. G. *Fractals in Chemistry*; Wiley-Interscience: New York, 1998.
(43) Birdi, K. S. *Fractals in Chemistry, Geochemistry, and Biophysics: An Introduction*; Plenum Publishing Corp.: New York, 1993.
(44) Sheintuch, M. *Catal. Rev.* **2001**, *43*, 233.
(45) Stockle, R. M.; Deckert, V.; Fokas, C.; Zeisel, D.; Zenobi, R. *Vib. Spectrosc.* **2000**, *22*, 39.
(46) Anderson, M. S.; Pike, W. T. *Rev. Sci. Instrum.* **2002**, *73*, 1198.
(47) Hayazawa, N.; Inouye, Y.; Sekkat, Z.; Kawata, S. *Opt. Commun.* **2000**, *183*, 333.
(48) Inouye, Y. *Top. Appl. Phys.* **2001**, *81*, 29.
(49) Nieman, L. T.; Krampert, G. M.; Martinez, R. E. *Rev. Sci. Instrum.* **2001**, *72*, 1691.
(50) Micic, M.; Klymyshyn, N.; Suh, Y., D.; Lu, H., P. *J. Phys. Chem. B* **2003**, *107*, 1574.
(51) Mackele, J. *Finite Elements Anal. Des.* **2001**, *37*, 575.
(52) Sun, Y.; Bell, T.; Zheng, S. *Thin Solid Films* **1995**, *258*, 198.
(53) Martin, Y. C.; Hamman, H. F.; Wickramasinghe, H. K. *J. Appl. Phys.* **2001**, *89*, 5774.
(54) Johnson, P. B.; Christy, R. W. *Phys. Rev. B* **1972**, *6*, 4372.
(55) Gianvittorio, J. P.; Rahmat-Samii, Y. *IEEE Antenna's and Propagation Magazine* **2002**, *44*, 20.
(56) Puente, C.; Claret, J.; Sagues, F.; Romcu, J.; Lopez-Salvans, M. Q.; Pous, R. *Electron. Lett.* **1996**, *32*, 2298.
(57) Milner, R. G.; Richard, D. *J. Microsc.—Oxford* **2001**, *202*, 66.
(58) Novotny, L.; Bian, R.; Xie, X. S. *Phys. Rev. Lett.* **1997**, *79*, 645.
(59) Krug, J. T.; Sanchez, E. J.; Xie, X. S.; Leung, P. T. *J. Chem. Phys.* **2002**, *116*, 10895.
(60) Kelly, L. K.; Coronado, E.; Zhao, L. L.; Schatz, G. C. *J. Phys. Chem. B* **2003**, *107*, 668.
(61) Hartschuh, A.; Sanchez, E. J.; Xie, X. S.; Novotny, L. *Phys. Rev. Lett.* **2003**, *90*, 095503.
(62) Suh, Y. D.; Schenter, G.; Zhu, L.; Lu, H. P. *Ultramicroscopy* **2003**, *97*, 89
(63) Walker, G. J.; James, J. R. *Electron. Lett.* **1998**, *34*, 1536.
(64) Weiss, A.; Haran, G. J. *J. Phys. Chem. B* **2001**, *105*, 12348.
(65) Cho, K. *Prog. Theor. Phys.: Supplement* **1991**, *106*, 225.
(66) Cho, K.; Ohfuti, Y.; Arima, K. *Jpn. J. Appl. Phys.* **1995**, *34 suppl.*, 267.
(67) Paule, E.; Reineker, P. *J. Phys. Chem. B* **2001**, *105*, 4293.
(68) Sanchez-Gil, J. A.; Garcia-Ramos, J. V. *J. Chem. Phys.* **1997**, *108*, 317.